

Accelerating Seafloor Uplift of Submarine Caldera near Sofugan Volcano, Japan, Resolved by Distant Tsunami Recordings

Tatsuya Kubota¹, Osamu Sandanbata², Tatsuhiko Saito¹, and Takanori Matsuzawa¹

¹National Research Institute for Earth Science and Disaster Resilience, Tsukuba, Japan

²Earthquake Research Institute, the University of Tokyo, Tokyo, Japan

Corresponding author: Tatsuya Kubota (kubotatsu@bosai.go.jp)

Key Points:

- We revealed the source kinematics of enigmatic tsunamis excited near Torishima on 8 October 2023 with the remote (> ~600 km) tsunami data.
- Its tsunami source was identified as repetitive seafloor uplift at the same location with gradually increasing amounts for later events.
- This unique feature of the accelerating caldera uplift within a few hours was brought about by the volcanic unrest of a submarine caldera.

Abstract

On 8 October 2023 UTC, significant tsunamis were observed around Japan without any major tsunamigenic earthquake, associated with a series of 14 successive minor earthquakes ($m_b = 4.5$ – 5.4) near Sofugan in the Izu-Bonin islands. To examine the cause of this tsunami, we estimated the horizontal locations of the tsunami source and temporal history of the seafloor displacement, using the tsunami data recorded by the ocean-bottom pressure gauges $> \sim 600$ km away. Our results showed the main tsunami source was an uplift located at a caldera-like bathymetric feature near Sofugan, suggesting the involvement of caldera activity in the tsunami generation. The total seafloor uplift was larger than ~ 3 m, and the uplift amount of each event gradually increased over time, reflecting an accelerating occurrence of multiple sudden caldera uplifts within only a few hours.

Plain Language Summary

On October 8, 2023, a tsunami was widely observed along the Japanese coast without any major tsunamigenic earthquake, while a series of small 14 earthquakes occurred near Sofugan, located in the Izu-Bonin islands. Two possible candidates for this tsunami have been proposed, submarine volcanic processes or submarine landslides, but the exact cause remains unclarified. Using the tsunami data observed by the seafloor pressure gauges located more than 600 km from the tsunami source region with an advanced technique, we analyzed sea height movements to obtain insights into the origin of this enigmatic tsunami. Our analysis showed that the tsunami source consisted of the seafloor uplift that repetitively occurred at a submarine volcanic caldera. Our results also showed an accelerating tsunami excitation, such that the amount of the seafloor uplift movement increased over time and the time intervals of the earthquakes gradually shortened. These results are consistent with the acceleration process of volcanic activity, suggesting the tsunami originated from the multiple sudden uplifts of the submarine caldera.

1 Introduction

On 8 October 2023 (UTC), tsunamis with maximum amplitudes of $> \sim 0.6$ m were observed along the Japanese coast without any major tsunamigenic earthquake. The Japan Meteorological Agency (JMA) issued a tsunami advisory for the Japanese coastal areas (JMA, 2023). JMA attributed the tsunami to an $M \sim 5$ earthquake at 20:25 near Sofugan, located ~ 80 km south of Torishima Island in the Izu-Bonin islands (Figure 1). Based on the earthquake catalog of the U.S. Geological Survey (USGS), 14 earthquakes with body wave magnitudes ranging from $m_b = 4.3$ to 5.7 were identified between 19:53 and 21:26 (circles in Figure 1). Hereafter, we sequentially refer to these events as Events 01 to 14 (Table 1).

Sandanbata et al. (2024) investigated the temporal history of the tsunami generation process. By analyzing the ocean-bottom pressure (OBP) gauge network installed in Southwestern Japan, the Dense Oceanfloor Network system for Earthquakes and Tsunamis (DONET) (Kaneda et al., 2015; Kawaguchi et al., 2015, Figure 1b), they proved that more than ten events that recurred for ~ 1.5 hours caused tsunamis successively, resulting in long-lasting and large-amplitude tsunamis. They also showed that these repetitive tsunamis were generated at the same timings as the occurrences of the earthquakes listed in the USGS catalog (Table 1) and high-frequency T-phase signals (> 1 Hz) in the OBP signals (seismic waves converted from oceanic acoustic waves propagating at a velocity of ~ 1.5 km/s; Okal, 2008). Based on the results, Sandanbata et al. (2024) proposed several possible candidates that generated this tsunami: a submarine volcanic process, such as eruptions, flank failures, intra-caldera faulting, or caldera collapse. However, their analysis focused on the temporal history of the tsunami generation process and could not reveal the source kinematics, leaving it difficult to determine the mechanism. To reveal and identify this unusual tsunami generation mechanism, it is required to quantify the location and the amount of seafloor deformation in addition to the temporal history.

In this study, we utilize the tsunami data observed by the OBP gauges around Japan to estimate the tsunami source location. Furthermore, we estimate the temporal evolution of the seafloor vertical deformation. Based on the results of the detailed seafloor bathymetry survey data, we examine and propose the cause of this abnormal tsunami event. In Section 2, we summarize the dataset used in this study. Section 3 analyzes the OBP data to estimate the horizontal location of the tsunami source. In Section 4, we constrain the amount of vertical

deformation due to each event during this sequence. Finally, we summarize the results and discuss the potential cause in Section 5.

2 Data

We use the OBP data from the Seafloor Observation Network for Earthquakes and Tsunamis along the Japan Trench (S-net) (Aoi et al., 2020) installed off northeastern Japan in addition to DONET (Figure 1), which are $> \sim 600$ km away from Sofugan. We suppress the ocean tide components using a theoretical tide model (Matsumoto et al., 2000) and then apply a bandpass filter with a passband of 100–500 s to remove the high-frequency seismic components and extract the tsunamis (Figure 2).

The arrival of the initial tsunami corresponds well to the theoretically expected one assuming the origin time of Event 01 (Figure S1), while the maximum amplitude was delayed by over 1 hour from the initial tsunami arrival. We also inspect the tsunami waveforms from an M_w 5.7 earthquake on 2 May 2015 (Fukao et al., 2018; Sandanbata et al., 2022), which occurred at the Sumisu caldera, located ~ 110 km north of Torishima Island (Figures S1 and S2). Compared to the 2015 tsunami, the amplitudes of the initial part were smaller but the later phases had much larger amplitudes, suggesting the successive tsunami generation by repetitive source events for the 8 October 2023 tsunami event. See Sandanbata et al. (2024) for more details on the features in the observed records.

Sandanbata et al. (2024) identified the significant T-phase signals corresponding to Events 01–13 in the DONET records, although the T-phase signal due to Event 14 was not identified. Our careful inspection of the seismograms around Japan confirmed the T-phase signal of Event 14 at the expected arrival time, although its amplitude was smaller than those of the other events (Figure S3, see Text S1 for details). Therefore, in the tsunami source modeling in the following section, we assume that Event 14 excited the tsunami as well as the other events (01–13).

3 Estimation of sea-surface displacements in each event

We estimate the distributions of the sea-surface vertical displacement (the tsunami source) due to Events 01–14, using the tsunami source inversion approach (e.g., Hossen et al., 2015; Kubota et al., 2021; Mizutani & Melger, 2023; Sandanbata et al., 2022; Tsushima et al., 2012). We here summarize the methodology of our analysis (see Text S2 and Figures S4–S6 for more details). We express the generation and propagation of tsunami by using two-dimensional linear dispersive tsunami wave equations with the Cartesian coordinates (e.g., Saito, 2019):

$$\frac{\partial \eta(\mathbf{x}, t)}{\partial t} = -\nabla \cdot (h \bar{\mathbf{v}}) + \dot{\eta}^S(\mathbf{x}, t) \quad (1)$$

and

$$\frac{\partial \bar{\mathbf{v}}(\mathbf{x}, t)}{\partial t} = -g_0 \nabla \eta + \frac{1}{3} h(\mathbf{x}) \frac{\partial}{\partial t} \nabla (\nabla \cdot (h \bar{\mathbf{v}})), \quad (2)$$

where $\eta = \eta(\mathbf{x}, t)$ is the sea-surface height change, $\bar{\mathbf{v}} = \bar{\mathbf{v}}(\mathbf{x}, t)$ is the horizontal velocity average over the water depth, $h = h(\mathbf{x})$ is the water depth, and $g_0 = 9.8 \text{ m/s}^2$ is the gravitational acceleration. The term $\dot{\eta}^S = \dot{\eta}^S(\mathbf{x}, t)$ generates the tsunami, which is the velocity of the sea-surface height excited by the N_t events (here, $N_t = 14$). This is represented by

$$\dot{\eta}^S(\mathbf{x}, t) = \sum_{k=1}^{N_t} \dot{\eta}_0^{(k)}(\mathbf{x}) \delta(t - T_k), \quad (3)$$

where $\eta_0^{(k)}(\mathbf{x})$ is the sea-surface height change due to the k -th event, $\delta(t)$ is the delta function, and T_k is the origin time of the k -th event.

In the practical analysis, we suppose that the waveforms at the n -th OBP located at $\mathbf{x}_n = (x_n, y_n)$, $p_n(t) = \rho_0 g_0 \eta(\mathbf{x}_n, t)$ (ρ_0 : the seawater density, $\sim 1.03 \text{ g/cm}^3$) can be represented by a linear superposition of the tsunami waveforms due to unit tsunami source elements of the sea-surface displacement $G_n^{(i,j)}(t)$ (hereafter referred to as the Green's functions), as:

$$p_n(t) = \sum_{i=1}^{N_x} \sum_{j=1}^{N_y} \sum_{k=1}^{N_t} m^{(i,j,k)} G_n^{(i,j)}(t - T_k), \quad (4)$$

where the parameter $m^{(i,j,k)}$ is the displacement amplitude of each of the unit source elements, which is to be estimated in the linear inversion problem, and N_x and N_y are the numbers of unit source elements in the spatial domain.

We assume the origin times of Events 01–14 (T_k) as those determined by USGS (Table 1; Figure S4). To calculate the Green's function from each source, we set the target area as 30 km \times 27 km (gray rectangle in Figure 1e) and distribute unit source elements ($N_x = 9$ and $N_y = 8$). Each source has a spatial extent of 6 km and the horizontal spatial intervals are 3 km. We then simulate a tsunami by solving a linear dispersive tsunami equation from the initial tsunami height distribution (e.g., Baba et al., 2015; Saito, 2019). We use the GEBCO2020 bathymetry data for the calculation, interpolating the spatial interval of $\Delta x = \Delta y = 1$ km (Figure S5). The time step interval of the simulation is $\Delta t = 1$ s, and the total number of the simulation steps is $N_{\text{step}} = 7,200$. We finally apply the same bandpass filter to the simulated waveform as that applied to the observation.

The time window used for the inversion analysis is set as 14,400 s from the origin time of Event 01. Based on visual inspection, we select the OBP stations to be used for the analysis (station names are written in blue text in Figure 2). All the DONET stations are used for the inversion, while we use only the S-net stations located south of 38°N. The inversion results are evaluated using the variance reduction (VR):

$$\text{VR} = \left(1 - \frac{\sum_n (p_n^{\text{obs}} - p_n^{\text{cal}})^2}{\sum_n p_n^{\text{obs}^2}} \right) \times 100 (\%). \quad (5)$$

Here, p_n^{obs} and p_n^{cal} indicate the n -th data of the observed and calculated waveforms. To stabilize the inversion, we consider the smoothing and damping constraints. The weights are determined based on the trade-off between the weights and the VR (Figure S6).

The total amount of the sea-surface displacement is shown in Figure 3b. Figures 3c to 3p are the distribution of the sea-surface height change due to each event (Events 01–14). The observations (black lines in Figure 2) are explained well by the simulation (red lines, VR = 57 %). The total displacement mainly had an uplift with a maximum amplitude of ~ 3 m (Figure 3b).

Sandanbata et al. (2024) considered that each event took place at the same location but at a different timing based on the similarity of the DONET tsunami signals. Mizutani and Melgar (2023) also conducted an inversion analysis to estimate the sea-surface height changes of the major events (Events 11, 12, and 13) and suggested these tsunami sources were located at the same location. Our results are consistent with these studies, but our results further suggest that the amounts of the uplift tend to be larger in the later events. We note that if we neglect the tsunami dispersion effect, the inversion results change significantly (Figures S7 and S8), indicating the necessity of considering the dispersion effect (e.g., Saito, 2019).

To evaluate the robustness of the inversion, we also conduct an additional inversion analysis (Figures S9 and S10, Text S2). We conduct the inversion imposing the constraint that sea-surface subsidence not be allowed (i.e., non-negative constraint, Lawson & Hanson, 1974), to evaluate the robustness of the subsidence for each event surrounding the main uplift regions. The other settings for the inversion are the same as above. The locations of the uplift are estimated as almost the same locations as the original result, and the agreement of the waveforms between the observation and simulation changed little ($VR = 53\%$). We cannot conclude whether this subsidence was real or just an artifact at this time. To better resolve the tsunami source, it should be necessary to use the shorter-period tsunami components (~ 100 s, Sandanbata, Watada, et al., 2021) or seismic waves (Sandanbata et al., 2022) for future work.

We can see a caldera-like seafloor bathymetric feature with a diameter of ~ 5 km, from a multibeam seafloor bathymetry survey result conducted in 1987 (Figures 1e and 3a), which corresponds to the location of the main uplift of the tsunami source (cross and circle in Figure 3). An urgent bathymetry survey in November 2023 by the Japan Agency for Marine-Earth Science and Technology (JAMSTEC) also confirmed the caldera at the same location (https://www.jamstec.go.jp/j/about/press_release/20231121/, in Japanese). Considering these bathymetric features and the temporal growth in the tsunami sources at the same location, we suggest that these seafloor uplifts due to each event should be brought by the volcanic activity of this submarine caldera. Note that the horizontal location of the event epicenters in the USGS catalog is located ~ 10 – 20 km west of this bathymetric feature, but this seems to be due to the uncertainty of the teleseismic hypocenter estimation (e.g., Wyss et al., 2011).

4 Estimation of seafloor uplift for each event

Assuming that the seafloor uplift repetitively took place at the caldera, we further examine the amount and temporal history of the uplift. In this analysis, we assume that the velocity of the vertical displacement at the seafloor $\dot{d}(\mathbf{x}, t)$ is expressed as:

$$\dot{d}(\mathbf{x}, t) = \sum_{k=1}^{N_t} d_0^{(k)}(\mathbf{x}) \delta(t - T_k), \quad (6)$$

where $d_0^{(k)}(\mathbf{x})$ is the seafloor displacement due to the k -th event, $\delta(t)$ is the delta function, and T_k is the origin time of the k -th event. The time history of the seafloor displacement is also expressed by the temporal integration:

$$d(\mathbf{x}, t) = \int_0^t \dot{d}(\mathbf{x}, t') dt'. \quad (7)$$

We assume a Gaussian-type seafloor vertical uplift (Saito & Furumura, 2009) for the seafloor displacement by each event, $d_0^{(k)}(\mathbf{x})$, as:

$$d_0^{(k)}(\mathbf{x}) = D_0^{(k)} \exp \left[-\frac{(x-x_0)^2 + (y-y_0)^2}{a^2} \right] \text{ for } k = 1, 2, \dots, N_t, \quad (8)$$

where a is the dimension that characterizes the horizontal scale of the distribution. We assume a is independent of k since our previous results suggested the same caldera displaced for all the events. $d_0^{(k)}(\mathbf{x})$ takes the maximum value of $D_0^{(k)}$ at $\mathbf{x}_0 = (x_0, y_0)$ (cross in Figure 1e). To estimate $D_0^{(k)}$ appropriately, we consider the effect of the spatial smoothing due to the seawater (Kajiura, 1963; Saito & Furumura, 2009), in which a small-scale spatial variation of the seafloor displacement is smoothened and disappears in the sea-surface deformation (see Text S3 and Figure S9 for the importance of this effect). We apply this filter to $d_0^{(k)}(\mathbf{x})$ assuming a seawater depth of $H = 1.5$ km (average depth around the source, Figure 1) to obtain the corresponding sea-surface displacement and to calculate the Green's functions. We then estimate $D_0^{(k)}$ by solving the inverse problem represented by Equation (1) ($N_x = N_y = 1$ and $N_t = 14$), without imposing

any constraint. We search for the optimum dimension of the source, by varying the dimension a ($= 2.5, 5.0, 7.5$, and 10 km).

We show the $D_0^{(k)}$ values of the optimum result in Figure 4 ($a = 7.5$ km, VR = 34 %, Figure S10). $D_0^{(k)}$ is larger in the later events, and the uplift increases over time as also pointed out in the tsunami source inversion (Figure 4; the minimum and maximum values are 9.5 cm for Event 01 and 48.3 cm for Event 13, respectively). This increasing feature of $D_0^{(k)}$ is almost consistent with the amplitude feature of the T-phase signals, recorded by the onshore seismometers (red and blue lines in Figure 4, see Text S1 and Figure S3 for more detail), although we note that the T-phase amplitude of Event 14 seems small compared to the significant $D_0^{(k)}$ of ~ 30 cm. We speculate that the generation mechanism of the T-phases might be diverse and complex within a series of events (e.g., Norris & Johnson, 1969; Okal, 2008; Sugioka et al., 2000). The cumulative uplift and the total volume of the uplift were estimated to be ~ 400 cm and $V = \iint_{-\infty}^{\infty} dx dy d(x, y) = d_0 \pi a^2 \sim 0.7$ km³. We also evaluate the uncertainty of $D_0^{(k)}$ depending on variations of the horizontal dimension of the Gaussian source a and the water depth H (Figure S11). Considering the uncertainty of the modeling, the amount of the total seafloor uplift should be larger than ~ 250 cm at least (Figure S11). We emphasize that the feature of the accelerating increase of the seafloor uplift remains the same.

5 Discussion and Conclusions

This study analyzed the tsunamis on 8 October 2023 near Sofugan, ~ 80 km south of Torishima Island, Japan, using waveforms recorded by the DONET and S-net OBPs (> 600 km). We obtained the spatio-temporal evolution of the sea-surface height changes (tsunami sources) based on the waveform inversion analysis. The results showed that the tsunami source was dominated by repetitive uplifts at the submarine volcanic caldera. The total amount of the seafloor uplift was estimated to be ~ 400 cm, and our results also suggested that the uplift increased over time from the initial event (the minimum uplift of 9 cm at Event 01) to a later event (the maximum of 48 cm at Event 13). This suggests the accelerating growth of the seafloor uplift.

Sandanbata et al. (2024) did not determine the cause of this tsunami but raised two possibilities: volcanic activity and seafloor landslides. The seafloor bathymetry survey results indicate the existence of the caldera at the tsunami source location (Figure 1e). Similar accelerating processes of repetitive events with decreasing inter-event times and increasing event magnitudes have been reported for the activity of the volcanic caldera (e.g., Michon et al., 2009; Wang et al., 2023). A report that a pumice raft was observed at ~50 km west of Sofugan on October 20 (<https://www.kaiho.mlit.go.jp/info/kouhou/post-1041.html>, in Japanese) also suggests the occurrence of volcanic activity. On the other hand, if the origin of this tsunami was landslides, a huge amount of the seafloor mass must have moved toward the caldera center from the surrounding area to explain the estimated large uplift at the caldera center; however, this seems unreasonable because this hypothesis should assume the mass moves from the surrounding area to the caldera center, which has a higher topography. In addition, no clear evidence of huge-scale landslides was confirmed in the bathymetric feature of the post-event survey (https://www.jamstec.go.jp/j/about/press_release/20231121/). Therefore, we conclude that the main cause of the tsunami is a series of seafloor uplifts related to the activity of the volcanic caldera near Sofugan.

At active volcanic calderas, trapdoor faulting, or sudden slip of the intra-caldera ring fault caused by overpressurization of its underlying magma reservoir, can cause sudden uplift of the caldera (Sandanbata et al., 2022; Sandanbata & Saito, 2024; Zheng et al., 2022), while a caldera collapse causes sudden subsidence of the caldera on a horizontal scale of the caldera structure (e.g., Acocella, 2007; Cole et al., 2005; Lipman, 1997). It has been often reported that submarine trapdoor faultings excite significant tsunamis, which have larger amplitudes than those expected from their seismic magnitudes (e.g., Fukao et al., 2018; Sandanbata et al., 2022; Sandanbata et al., 2023). Another characteristic feature of trapdoor faultings is that they have large non-double-couple (non-DC) components in the centroid moment tensor (CMT) solution, associated with the curved fault geometry at the ring-faulting (Sandanbata, Kanamori, et al., 2021). Although only two CMT solutions of Events 01 and 03 are available in the USGS catalog, they have large non-DC components (Figure 1e). These points may suggest the successive occurrence of trapdoor faulting at the caldera. If the trapdoor faulting mechanism is the origin of this seafloor uplift, the repetitive and accelerating occurrence of the multiple tsunamigenic events within a few hours seems to be unique, whereas the past events consisted of only a single

event. In cases of a subaerial caldera of Sierra Negra volcano, Galápagos Islands, trapdoor faulting causing sudden caldera uplift preceded the initiations of caldera eruptions in 2005 and 2018 (e.g., Jónsson, 2009; Geist et al., 2008; Bell et al., 2021; Shreve & Delgado, 2023), suggesting the potential for triggering eruptions. To understand the whole process of this unique caldera activity, it is necessary to continuously and repetitively monitor the long-term post-event process using seafloor bathymetry survey (e.g., Fujiwara, 2021; Kodaira et al., 2021) as well as geodetic observation (e.g., Chadwick et al., 1999; 2012).

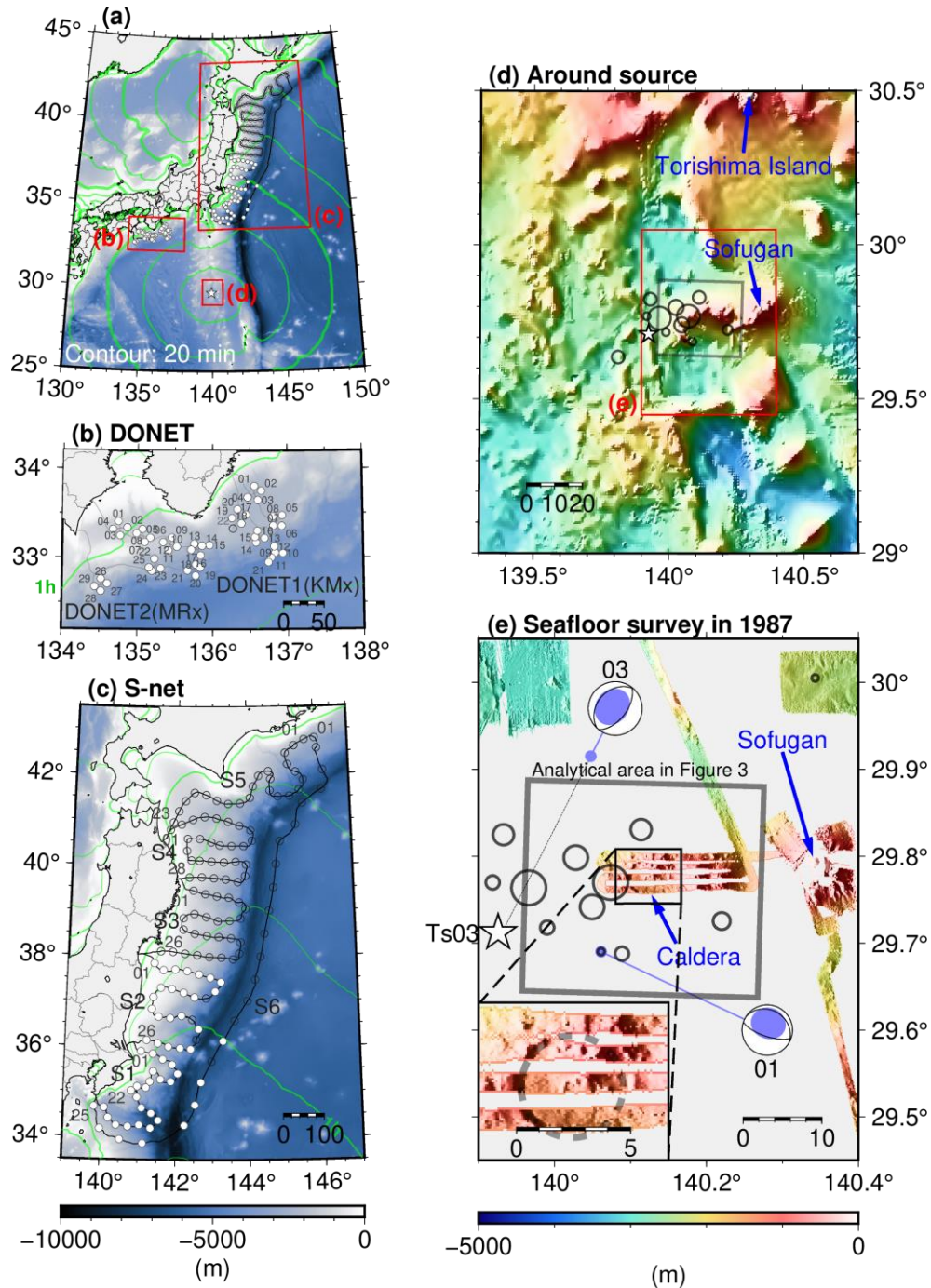


Figure 1. (a) Location map of this study. The epicenter of Event 03 is shown by a star. Green contour lines denote expected tsunami travel times (20-min intervals). (b, c) Location maps of DONET and S-net. (d) Close-up view around the source region. Circles denote the epicenters of the events from the USGS catalog. (e) Seafloor bathymetry around Sofugan. The CMT solutions of Events 01 and 03 (USGS) are also shown. The inset map shows the region ~20 km west of Sofugan.

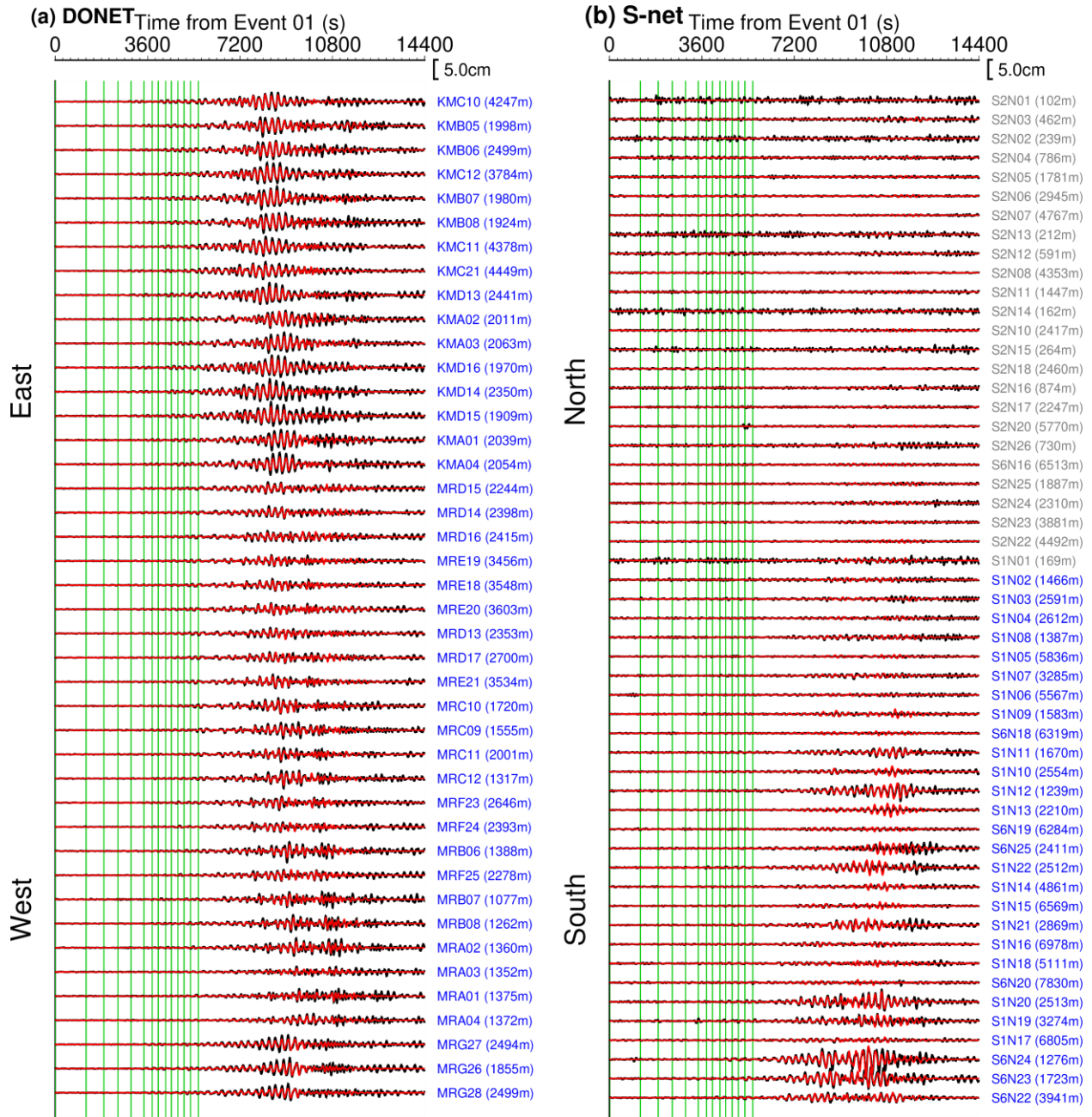


Figure 2. Tsunami waveforms at the (a) DONET and (b) S-net OBPs. Black and red lines are the observed waveforms and the calculated waveforms from the tsunami source inversion, respectively. Stations shown in blue text are used for the inversion analysis. Installation depths of the OBPs are also shown. Note that a 1 cm sea-surface height change is assumed to be equivalent to a 1 hPa seafloor pressure change.

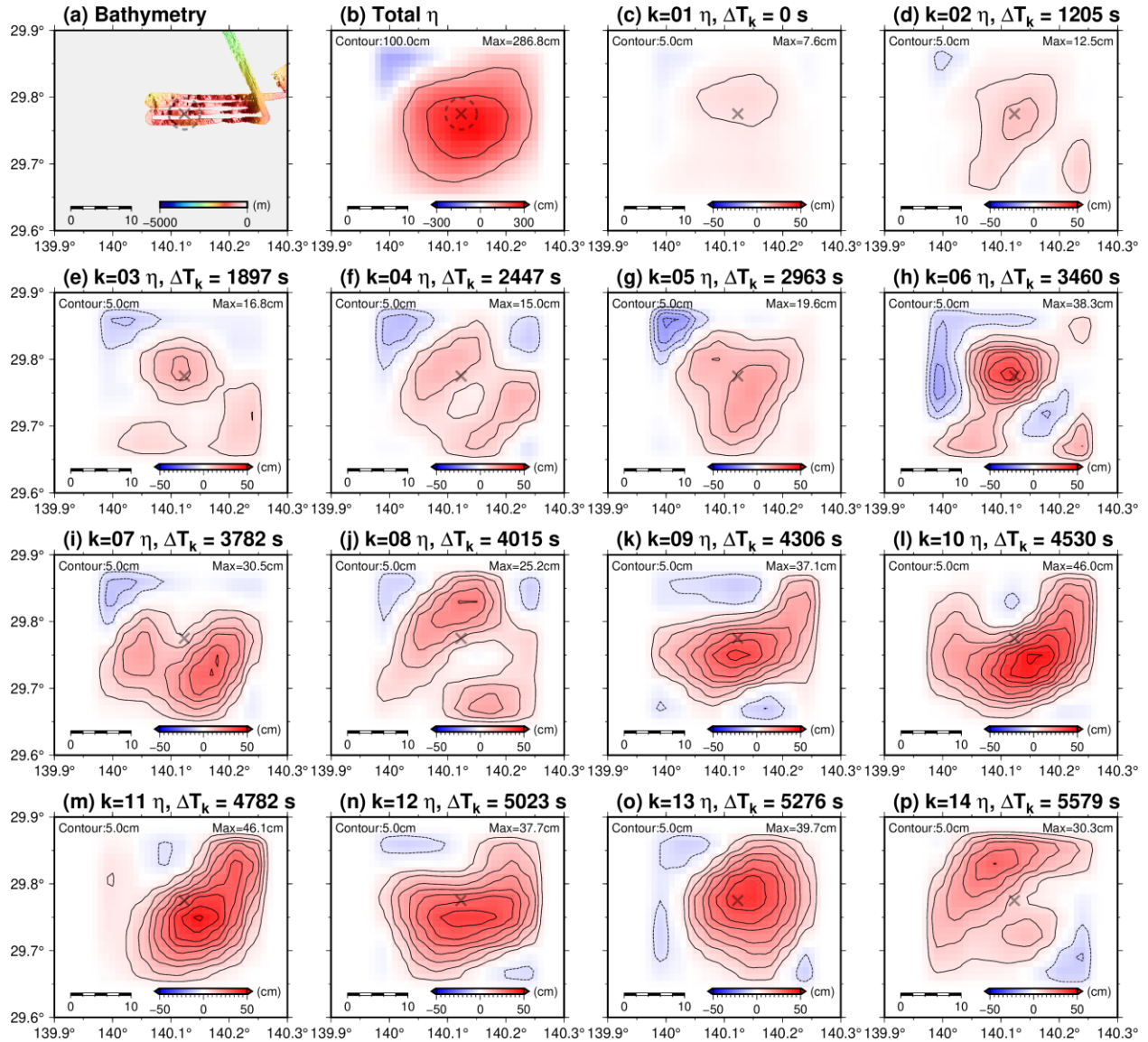


Figure 3. Distribution of the static sea-surface displacement. (a) Seafloor bathymetry around the source region. The caldera-like seafloor bathymetry is marked by a circle with a dashed line, and its center is marked by a cross. (b) Final displacement of the seafloor. (c–p) Displacements due to each event. The relative time from Event 01, ΔT_k , is also shown.

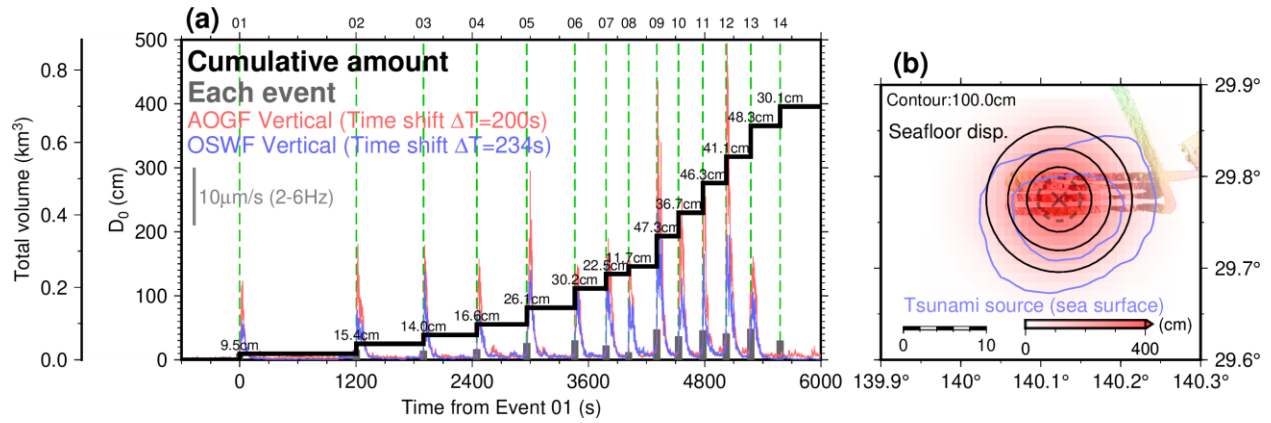


Figure 4. (a) Temporal history of $D_0^{(k)}$ values (gray bars). The cumulative $D_0^{(k)}$ is also shown by a black line. Red and blue waveforms are the envelope waveforms of the 2–6 Hz vertical component at the onshore seismometers at Aogashima Island and Ogasawara Island, respectively (see Figure S3 for their locations), which are manually shifted so that their T-phase arrivals roughly coincide with the origin times. (b) The total seafloor uplift distribution of the optimum model (black contour, 0.2 m intervals). The total sea-surface uplift obtained by the inversion (Figure 3b) is also shown by blue contours.

311 **Table 1.** List of the events during the Torishima sequence on 8 October 2023 UTC.

Event ID	Origin time (hh:mm:ss.sss)	Longitude (E°)	Latitude (N°)	Depth (km)	m_b	M_w^b	Time from Event 01, ΔT_k (s)	Earthquake event # in Sandanbata et al. (2024) ^c
01	19:53:46.086	140.0613	29.6904	10	4.5	4.4	0	Se02
02	20:13:50.973	140.0888	29.6880	10	4.7		1205	Se03
03 ^a	20:25:22.652	139.9258	29.7121	10	4.7	4.7	1897	Se04
04	20:34:32.705	139.9904	29.7181	10	4.7		2447	Se05
05	20:43:09.456	140.2201	29.7256	10	4.8		2963	Se06
06	20:51:25.664	139.9186	29.7700	10	4.7		3460	Se07
07	20:56:48.379	139.9328	29.8249	10	4.9		3782	Se08
08	21:00:40.543	140.0495	29.7418	10	5.0		4015	Se09
09	21:05:32.437	139.9661	29.7638	10	5.4		4306	Se10
10	21:09:16.452	140.1140	29.8308	10	4.9		4530	Se11
11	21:13:27.937	140.0281	29.7985	10	5.0		4782	Se12
12	21:17:28.430	140.0739	29.7700	10	5.3		5023	Se13
13	21:21:41.729	139.8132	29.6373	10	4.9		5276	Se14
14	21:26:45.096	140.3431	30.0050	10	4.5		5579	Se15

312 ^aEvent 03 was reported as the event that caused the tsunami (JMA, 2023).313 ^bCMT solutions of only Events 01 and 03 are available in the USGS catalog (Figure 1e).314 ^cSee Table S1 of Sandanbata et al. (2024). Note that the earthquake event Se01 did not excite a
315 significant tsunami and thus was not modeled in this study.

316

Acknowledgments

Discussions with Gou Fujie, Toshiya Fujiwara, Ayumu Mizutani, Azusa Nishizawa, and Lina Yamaya were fruitful. This work was financially supported by JSPS KAKENHI Grant Numbers 22K14126 and 23H01666.

Open Research

Data Availability Statement

The catalog of earthquakes and CMT solutions is available from the USGS website (<https://www.usgs.gov/programs/earthquake-hazards/earthquakes>). The DONET and S-net OBP data of the National Research Institute for Earth Science and Disaster Resilience (NIED) (NIED, 2019a; 2019b, <https://www.seafloor.bosai.go.jp>, only available in Japanese) are available on request and with permission through <https://hinetwww11.bosai.go.jp/auth/oc/> (only available in Japanese). The seismogram data of DONET, F-net, and Hi-net (NIED, 2019a; 2019c; 2019d) are available through <https://hinetwww11.bosai.go.jp/auth/?LANG=en>. To access all the NIED data the user registration is necessary (<https://hinetwww11.bosai.go.jp/nied/registration/?LANG=en>). The data policy of NIED is available at <https://www.mowlas.bosai.go.jp/policy/?LANG=en>. The GEBCO2020 bathymetry data (GEBCO Bathymetric Compilation Group 2020, 2020) was downloaded from https://www.gebco.net/data_and_products/historical_data_sets/#gebco_2020. The bathymetry survey data in 1987 (Figures 1e and 3a, https://www.ngdc.noaa.gov/ships/atlantis_ii/AII8L18_mb.html) was downloaded from the bathymetric data viewer of the National Oceanic and Atmospheric Administration (NOAA) (NOAA National Centers for Environmental Information, 2004; <https://www.ncei.noaa.gov/maps/bathymetry/>).

The calculation of the theoretical travel time tsunami was conducted by Geoware TTT software version 3.2, which was purchased through Geoware Online (<http://www.geoware-online.com/tsunami.html>). The theoretical tide model NAO.99Jb (Matsumoto et al., 2000) is available from https://www.miz.nao.ac.jp/staffs/nao99/index_En.html. The Seismic Analysis Code (SAC) software was used for data processing (Goldstein et al., 2003). Figures were prepared using the Generic Mapping Tools Version 6 (GMT6) software (Wessel et al., 2019).

All the websites in this manuscript were accessed on 1 January 2024.

References

- Acocella, V. (2007). Understanding caldera structure and development: An overview of analogue models compared to natural calderas. *Earth-Science Reviews*, 85, 125–160. <https://doi.org/10.1016/j.earscirev.2007.08.004>
- Aoi, S., Asano, Y., Kunugi, T., Kimura, T., Uehira, K., Takahashi, N., & Ueda, H. (2020). MOWLAS : NIED observation network for earthquake, tsunami and volcano. *Earth, Planets and Space*, 72, 126. <https://doi.org/10.1186/s40623-020-01250-x>
- Baba, T., Takahashi, N., Kaneda, Y., Ando, K., Matsuoka, D., & Kato, T. (2015). Parallel implementation of dispersive tsunami wave modeling with a nesting algorithm for the 2011 Tohoku Tsunami. *Pure and Applied Geophysics*, 172(12), 3455–3472. <https://doi.org/10.1007/s00024-015-1049-2>
- Bell, A. F., LaFemina, P. C., Ruiz, M., Amelung, F., Bagnardi, M., Bean, C. J., et al. (2021b). Caldera resurgence during the 2018 eruption of Sierra Negra Volcano, Galápagos Islands. *Nature Communications*, 12, 1397. <https://doi.org/10.1038/s41467-021-21596-4>
- Chadwick, W. W. Jr., Embley, R. W., Milburn, H. B., Meinig, C., & Stapp, M. (1999). Evidence for deformation associated with the 1998 eruption of Axial Volcano, Juan de Fuca Ridge, from acoustic extensometer measurements. *Geophysical Research Letters*, 26(23), 3441–3444. <https://doi.org/10.1029/1999GL900498>
- Chadwick, W. W., Nooner, S. L., Butterfield, D. A., & Lilley, M. D. (2012). Seafloor deformation and forecasts of the April 2011 eruption at Axial Seamount. *Nature Geoscience*, 5, 474–477. <https://doi.org/10.1038/ngeo1464>
- Cole, J. W., Milner, D. M., & Spinks, K. D. (2005). Calderas and caldera structures: A review. *Earth-Science Reviews*, 69(1–2), 1–26. <https://doi.org/10.1016/j.earscirev.2004.06.004>
- Fujiwara, T. (2021). Seafloor geodesy from repeated multibeam bathymetric surveys: application to seafloor displacement caused by the 2011 Tohoku-Oki earthquake. *Frontiers in Earth Science*, 9, 667666. <https://doi.org/10.3389/feart.2021.667666>
- Fukao, Y., Sandanbata, O., Sugioka, H., Ito, A., Shiobara, H., Watada, S., & Satake, K. (2018). Mechanism of the 2015 volcanic tsunami earthquake near Torishima, Japan. *Science Advances*, 4(4), eaao0219. <https://doi.org/10.1126/sciadv.aao0219>

- GEBCO Bathymetric Compilation Group 2020 (2020). The GEBCO_2020 Grid – a continuous terrain model of the global oceans and land [Dataset]. British Oceanographic Data Centre, National Oceanography Centre, NERC, UK. <https://doi.org/10.5285/a29c5465-b138-234d-e053-6c86abc040b9>
- Geist, D. J., Harpp, K. S., Naumann, T. R., Poland, M., Chadwick, W. W., Hall, M., & Rader, E. (2008). The 2005 eruption of Sierra Negra volcano, Galápagos, Ecuador. *Bulletin of Volcanology*, 70(6), 655–673. <https://doi.org/10.1007/s00445-007-0160-3>
- Goldstein, P., Dodge, D., Firpo, M., & Minner, L. (2003). SAC2000: Signal processing and analysis tools for seismologists and engineers. In W. H. K. Lee, H. Kanamori, P. C. Jennings, & C. Kisslinger (Eds.), Eds., *International Handbook of Earthquake and Engineering Seismology* (Vol. 81, pp. 1613–1614). London: Academic Press. [https://doi.org/10.1016/S0074-6142\(03\)80284-X](https://doi.org/10.1016/S0074-6142(03)80284-X)
- Hossen, M. J., Cummins, P. R., Dettmer, J., & Baba, T. (2015). Tsunami waveform inversion for sea surface displacement following the 2011 Tohoku earthquake: Importance of dispersion and source kinematics. *Journal of Geophysical Research: Solid Earth*, 120(9), 6452–6473. <https://doi.org/10.1002/2015JB011942>
- Japan Meteorological Agency (2023). Report on Earthquake near Torishima Island around 5:25 on October 9, 2023 (2nd report) (in Japanese). Retrieved October 19, 2023, from <https://www.jma.go.jp/jma/press/2310/09b/202310091100.html>
- Jónsson, S. (2009). Stress interaction between magma accumulation and trapdoor faulting on Sierra Negra volcano, Galápagos. *Tectonophysics*, 471(1), 36–44. <https://doi.org/10.1016/j.tecto.2008.08.005>
- Kajiura, K. (1963). The leading wave of a tsunami. *Bulletin of the Earthquake Research Institute*, 41, 535–571. <https://doi.org/10.15083/0000033711>
- Kaneda, Y., Kawaguchi, K., Araki, E., Matsumoto, H., Nakamura, T., Kamiya, S., et al. (2015). Development and application of an advanced ocean floor network system for megathrust earthquakes and tsunamis. In P. Favali, L. Beranzoli, & A. De Santis (Eds.), *Seafloor Observatories: A new vision of the Earth from the Abyss* (pp. 643–662). Berlin, Heidelberg: Springer. https://doi.org/10.1007/978-3-642-11374-1_25
- Kawaguchi, K., Kaneko, S., Nishida, T., & Komine, T. (2015). Construction of the DONET real-time seafloor observatory for earthquakes and tsunami monitoring. In P. Favali, L.

- Beranzoli, & A. De Santis (Eds.), *Seafloor Observatories: A New Vision of the Earth from the Abyss* (pp. 211–228). https://doi.org/10.1007/978-3-642-11374-1_10
- Kikuchi, M., & Kanamori, H. (1982). Inversion of complex body waves. *Bulletin of the Seismological Society of America*, 72(2), 491–506.
<https://doi.org/10.1785/BSSA0720020491>
- Kodaira, S., Fujiwara, T., Fujie, G., Nakamura, Y., & Kanamatsu, T. (2020). Large coseismic slip to the trench during the 2011 Tohoku-Oki earthquake. *Annual Review of Earth and Planetary Sciences*, 48, 321–343. <https://doi.org/10.1146/annurev-earth-071719-055216>
- Kubota, T., Saito, T., Tsushima, H., Hino, R., Ohta, Y., Suzuki, S., & Inazu, D. (2021). Extracting near-field seismograms from ocean-bottom pressure gauge inside the focal area: Application to the 2011 Mw 9.1 Tohoku-Oki earthquake. *Geophysical Research Letters*, 48, e2020GL091664. <https://doi.org/10.1029/2020GL091664>
- Lawson, C. L., & Hanson, B. J. (1974). *Solving least squares problems*. Englewood Cliffs, NJ: Prentice-Hall.
- Lipman, P. W. (1997). Subsidence of ash-flow calderas: relation to caldera size and magma-chamber geometry. *Bulletin of Volcanology*, 59, 198–218.
<https://doi.org/10.1007/s004450050186>
- Matsumoto, K., Takanezawa, T., & Ooe, M. (2000). Ocean tide models developed by assimilating TOPEX/POSEIDON altimeter data into hydrodynamical model: A global model and a regional model around Japan. *Journal of Oceanography*, 56, 567–581.
<https://doi.org/10.1023/A:1011157212596>
- Michon, L., Villeneuve, N., Catry, T., & Merle, O. (2009). How summit calderas collapse on basaltic volcanoes: New insights from the April 2007 caldera collapse of Piton de la Fournaise volcano. *Journal of Volcanology and Geothermal Research*, 184(1), 138–151. <https://doi.org/10.1016/j.jvolgeores.2008.11.003>
- Mizutani, A., & Melgar, D. (2023). Potential volcanic origin of the 2023 short-period tsunami in the Izu Islands, Japan. *Seismica*, 2(2). <https://doi.org/10.26443/seismica.v2i2.1160>
- National Research Institute for Earth Science and Disaster Resilience (2019a). NIED DONET [Dataset]. National Research Institute for Earth Science and Disaster Resilience.
<https://doi.org/10.17598/nied.0008>

- National Research Institute for Earth Science and Disaster Resilience (2019b). NIED S-net.
National Research Institute for Earth Science and Disaster Resilience.
<https://doi.org/10.17598/nied.0007>
- National Research Institute for Earth Science and Disaster Resilience (2019c). NIED F-net
[Dataset]. National Research Institute for Earth Science and Disaster Resilience.
<https://doi.org/10.17598/nied.0005>
- National Research Institute for Earth Science and Disaster Resilience (2019d). NIED Hi-net
[Dataset]. National Research Institute for Earth Science and Disaster Resilience.
<https://doi.org/10.17598/nied.0003>
- NOAA National Centers for Environmental Information (2004). Multibeam Bathymetry
Database (MBBDB) [Dataset]. NOAA National Centers for Environmental Information.
<https://doi.org/doi:10.7289/V56T0JNC>.
- Norris, R.A., & Johnson, R. H. (1969). Submarine volcanic eruptions recently located in the
Pacific by Sofar Hydrophones. *Journal of Geophysical Research*, 74(2), 650-664.
<https://doi.org/10.1029/JB074i002p00650>
- Okal, E. A. (2008). The generation of *T* waves by earthquakes. *Advances in Geophysics*, 49, 1–
65. [https://doi.org/10.1016/S0065-2687\(07\)49001-X](https://doi.org/10.1016/S0065-2687(07)49001-X)
- Paris, R. (2015). Source mechanisms of volcanic tsunamis. *Philosophical Transactions of The
Royal Society A: Mathematical, Physical, and Engineering Sciences*, 373, 20140380.
<https://doi.org/10.1098/rsta.2014.0380>
- Saito, T. (2019). *Tsunami generation and propagation*. Tokyo: Springer Tokyo.
<https://doi.org/10.1007/978-4-431-56850-6>
- Saito, T., & Furumura, T. (2009). Three-dimensional tsunami generation simulation due to sea-
bottom deformation and its interpretation based on the linear theory. *Geophysical
Journal International*, 178, 877–888. <https://doi.org/10.1111/j.1365-246X.2009.04206.x>
- Sandanbata, O., Kanamori, H., Rivera, L., Zhan, Z., Watada, S., & Satake, K. (2021). Moment
tensors of ring-faulting at active volcanoes: Insights into vertical-CLVD earthquakes at
the Sierra Negra Caldera, Galápagos Islands. *Journal of Geophysical Research: Solid
Earth*, 126, 2021JB021693. <https://doi.org/10.1029/2021JB021693>
- Sandanbata, O., & Saito, T. (2024). Quantifying magma overpressure beneath a submarine
caldera: A mechanical modeling approach to tsunamigenic trapdoor faulting near Kita-

- Ioto Island, Japan. *Journal of Geophysical Research: Solid Earth*, 129, e2023JB27917.
<https://doi.org/10.1029/2023JB027917>
- Sandanbata, O., Satake, K., Takemura, S., Watada, S., Maeda, T., & Kubota, T. (2024).
 Enigmatic tsunami waves amplified by repetitive source events near Sofugan volcano,
 Japan. *Geophysical Research Letters*, 51, e2023GL106949.
<https://doi.org/10.1029/2023GL106949>
- Sandanbata, O., Watada, S., Ho, T.-C., & Satake, K. (2021). Phase delay of short-period
 tsunamis in the density-stratified compressible ocean over the elastic Earth. *Geophysical
 Journal International*, 226, 1975–1985. <https://doi.org/10.1093/gji/ggab192>
- Sandanbata, O., Watada, S., Satake, K., Kanamori, H., & Rivera, L. (2023). Two volcanic
 tsunami events caused by trapdoor faulting at a submerged caldera near Curtis and
 Cheeseman islands in the Kermadec arc. *Geophysical Research Letters*, 50,
 e2022GL101086. <https://doi.org/10.1029/2022GL101086>
- Sandanbata, O., Watada, S., Satake, K., Kanamori, H., Rivera, L., & Zhan, Z. (2022). Sub-
 decadal volcanic tsunamis due to submarine trapdoor faulting at Sumisu caldera in the
 Izu–Bonin Arc. *Journal of Geophysical Research: Solid Earth*, 127, e2022JB024213.
<https://doi.org/10.1029/2022JB024213>
- Shreve, T., & Delgado, F. (2023). Trapdoor fault activation: A step toward caldera collapse at
 Sierra Negra, Galápagos, Ecuador. *Journal of Geophysical Research: Solid Earth*, 128,
 e2023JB026437. <https://doi.org/10.1029/2023JB026437>
- Sugioka, H., Fukao, Y., Kanazawa, T., & Kanjo, K. (2000). Volcanic events associated with an
 enigmatic submarine earthquake. *Geophysical Journal International*, 142(2), 361–370.
<https://doi.org/10.1046/j.1365-246x.2000.00153.x>
- Tsushima, H., Hino, R., Tanioka, Y., Imamura, F., & Fujimoto, H. (2012). Tsunami waveform
 inversion incorporating permanent seafloor deformation and its application to tsunami
 forecasting. *Journal of Geophysical Research*, 117, B03311.
<https://doi.org/10.1029/2011JB008877>
- Wang, T. A., Segall, P., Hotovec-Ellis, A. J., Anderson, K. R., & Cervelli, P. F. (2023). Ring
 fault creep drives volcano-tectonic seismicity during caldera collapse of Kīlauea in
 2018. *Earth and Planetary Science Letters*, 618, 118288.
<https://doi.org/10.1016/j.epsl.2023.118288>

Wessel, P., Luis, J. F., Uieda, L., Scharroo, R., Wobbe, F., Smith, W. H. F., & Tian, D. (2019).
The Generic Mapping Tools Version 6. *Geochemistry, Geophysics, Geosystems*, 20,
5556–5564. <https://doi.org/10.1029/2019GC008515>

Wyss, M., Elashvili, M., Jorjiashvili, N., & Javakhishvili, Z. (2011). Uncertainties in teleseismic
earthquake locations: implications for real-time loss estimates. *Bulletin of the
Seismological Society of America*, 101, 1152–1161. <https://doi.org/10.1785/0120100168>

Zheng, Y., Blackstone, L., & Segall, P. (2022). Constraints on absolute magma chamber volume
from geodetic measurements of trapdoor faulting at Sierra Negra volcano, Galapagos.
Geophysical Research Letters, 49, 2021GL095683.
<https://doi.org/10.1029/2021GL095683>